Experimental and Theoretical Studies on Friction Contact of Bolted Joint Interfaces

Original
Experimental and Theoretical Studies on Friction Contact of Bolted Joint Interfaces / Li, D., Botto, D., Li, R., Xu, C., Zhang, W.. - In: INTERNATIONAL JOURNAL OF MECHANICAL SCIENCES. - ISSN 0020-7403. - ELETTRONICO. - 236:(2022), p. 107773. [10.1016/j.ijmecsci.2022.107773]

Publisher:
Elsevier

Published
DOI:10.1016/j.ijmecsci.2022.107773

https://doi.org/10.1016/j.ijmecsci.2022.107773

Experimental and Theoretical Studies on Friction Contact of Bolted Joint Interfaces

Dongwu Li[1], Daniele Botto[2], Ruozhang Li[1], Chao Xu[3], Wenming Zhang[1*]

[1]State Key Laboratory of Mechanical System and Vibration, School of Mechanical Engineering,
Shanghai Jiao Tong University Shanghai, 200240, China
[2]Department of Mechanical and Aerospace Engineering, Politecnico di Torino, Turin 10129, Italy
[3]School of Astronautics, Northwestern Polytechnical University, Xi'an 710072, China

Abstract: This paper presents experimental and theoretical modeling studies on the tangential contact stiffness and friction hysteresis of bolted joint interfaces under transversal vibration. A new test rig was developed to measure the interface fretting response of bolted joints. This rig is based on a servo-hydraulic fatigue testing system in which the contact surfaces are arranged symmetrically to avoid bending of the specimen that could affect the friction measurement. Force-displacement curves were measured under different tangential loads and compared with those found in the literature. A multi-scale contact modeling method was proposed to calculate the tangential contact stiffness and reproduce the friction hysteresis of bolted joint interfaces. This method overcomes the complexity of identifying contact stiffness, which usually requires a model of the dynamic behavior of the joint and frequency responses measured with dedicated fretting test stands. Specifically, this method comprehensively considers the multi-scale features of randomly rough surfaces, the non-uniform contact pressure distribution, and the convenience of phenomenological contact models in simulating frictional hysteresis, relying on fractal contact theory and discretized Iwan model. The effectiveness of the proposed method was verified by comparing the simulation results with the experimental counterparts in different cases of tangential loading. The successful validation demonstrates the potential of the proposed modeling method for application to structures with bolted joint.

Keywords: Bolted joint; friction hysteresis; contact stiffness; fractal theory; Iwan model.

---

[*] Corresponding author: wenmingz@sjtu.edu.cn (wenming Zhang)

1 Introduction

Bolted joints are widely used in various mechanical systems, such as turbine engines, spacecraft, wind turbines, etc., to make two or more components assembled as a whole and transmit loads. Subjected to transversal vibration, the mechanical behavior induced by the relative motion of the bolted joint interface exhibits nonlinear stiffness and energy dissipation characteristics (i.e. frictional hysteresis) [1-5]. The contact condition of the interface (possibly stick, partial slip, and gross slip) is related to the level of transversal vibration. This inherent nonlinearity of friction can cause the 'frequency shift' and instability in the dynamic response of assembled structures, which may further lead to undesired resonance and increase the difficulty of structural control [6-11]. Therefore, an accurate description of interface frictional hysteresis behavior is of great importance for dynamic modeling and vibration control of assembled structures.

Extensive experimental and theoretical studies have been carried out to understand the contact mechanisms of bolted joints and to characterize the interface friction hysteresis. The work by Gaul et al. [12] is considered one of the milestones in the field of joint structural mechanics. They investigated the hysteresis response of the bolted interface through a mixed experimental and numerical strategy and discussed the effects of excitation amplitude and bolt preload on the hysteresis behavior. Eriten et al. [13] compared hysteresis curves and energy dissipation between steel and aluminum jointed samples and obtained the same exponential relationship between energy dissipation per cycle and the maximum tangential force as obtained in Ref. [14][15]. Subsequently, they studied the effects of surface roughness and lubrication on the hysteresis behavior of bolted joints, revealing the underlying mechanism affecting the friction force, contact stiffness, and damping [16]. Li et al. [17][18] studied the effect of load level and fretting wear on the friction hysteresis curve and contact parameters (contact stiffness and friction coefficient). Moreover, a theoretical contact analysis was performed to demonstrate that the residual stiffness phenomenon (found in the gross slip regime) is due to the influence of other contact surfaces in bolted joints. Recently, Zhao et al. [19] emphasized, by experiments and finite element analysis, the role of contact pressure distribution in the nonlinear softening of the tangential contact stiffness of bolted joint. From the above experimental studies, it can be found that there are many factors affecting the interface hysteresis of bolted joints. Therefore, it is still a challenge to comprehensively consider these factors in modeling the friction hysteresis of bolted joints.

Generally, there are mainly two families of modeling methods applied to simulate the friction contact behavior: models that account for rough contact (physics-based models) and phenomenological contact models (data-driven models). Models with rough contact characterize a rough surface as a collection of many asperities (in single-scale [20-22] or multi-scale [23-27]). The overall contact behavior of the interface is obtained by combining the deformation features of a single asperity with statistical methods. These methods consider the rough surface characteristics and physics-based constitutive relation. However, since the force-displacement expression obtained is not explicit, it is unlikely to be compatible with a structural dynamic analysis code.

In comparison, the phenomenological models, such as Iwan model [28-32], Valanis model [12][33], and LuGre model [34], can be easily integrated into the joint structural dynamic analysis method due to good compatibility. Especially, due to the generality of the model parameters (contact stiffness and friction coefficient) and the simple expression of the force-displacement nonlinear relation, the Iwan model has wide application in dynamic modeling of jointed structures. In its first iterations, the Iwan density function - the core of the Iwan model - is assumed to be a truncated power-law distribution with a Dirac delta function [28][30][35]. These models have 4-6 parameters that must be obtained by fitting the results of appropriate experiments, which partially limits the application of the model. Li et al. [36][37] proposed a mapping relationship from the contact pressure distribution to the Iwan density function without introducing new parameters. This model requires only two parameters, contact stiffness and friction coefficient. Li et al. [38] improved the Iwan model using similar ideas and developed a parameter identification method. Although these improved Iwan models show good accuracy in the simulation of friction hysteresis and have good compatibility with structural dynamic analysis, the model parameters estimation procedure is inconvenient for predicting dynamic response of jointed structures. Actually, this procedure requires dedicated fretting test rigs or measured frequency response curves [39-44].

The objective of this work is to develop a method for modeling friction contact to facilitate the dynamic analysis of jointed structures without resorting to dedicated friction tests or dynamic tests.

This method comprehensively considers the multi-scale features of randomly rough surfaces, the non-uniform distribution of contact pressure, and the convenience of phenomenological contact models in friction hysteresis simulation. At the same time, to verify the effectiveness of the proposed method, a new fretting test rig was developed. This test rig was specially designed to avoid the effects of residual stiffness and to eliminate as much as possible the effect of additional moments during reaching the contact conditions on the jointed interfaces.

The remainder of this paper is organized as follows. Section 2 describes the newly developed fretting test apparatus and shows the experimental hysteresis curves under different loads. Section 3 presents the multi-scale modeling approach to calculate the tangential contact stiffness of jointed interfaces and reproduce friction hysteresis behavior. Section 4 verifies the effectiveness of the proposed modeling approach by comparison of the simulation results with the experimental counterparts, and discusses the effect of the interface discretization on the model performance. Section 5 closes the paper by highlighting the novelty of the proposed method and presenting the main conclusions.

2 Experimental tests

2.1 Experimental method

Figure 1(a and b) shows an overview and a photograph of the test apparatus used in the experiments. To capture the friction force of bolted joint interface as purely as possible, the joint sample with two moving specimens and a fixed specimen is arranged in a symmetric layout. As a comparison, the friction force measured in an asymmetric layout is mixed with that at other interfaces (between the screw head, the washer, the nut and the target interface) and the bending deformation of the bolt shank, which introduces errors into friction measurement [17], as shown in Fig. 1(c and d). Ref. [17] developed a theoretical model to analyze these factors and attributed the origin of the residual stiffness (i.e. the slope of the displacement-force curve during the gross slip regime) to them. In this experiment, to avoid the influence of the above factors on friction measurement, a symmetric specimen layout is adopted. Additionally, the experimental results are available for indirectly verifying the theoretical analyses in Ref. [17] where some ideal assumptions were employed.

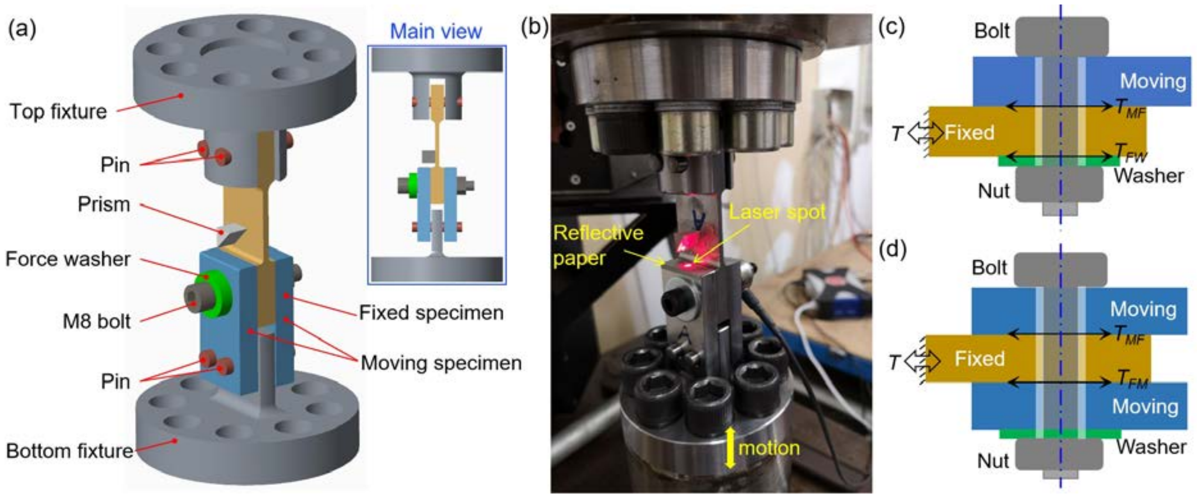

Fig. 1 (a) Schematic diagram of the fretting test apparatus and main components, (b) photograph of the servo-hydraulic fatigue testing system and the assembled bolted joint specimens. The joint specimens are periodically displaced long the piston shaft. (c) Asymmetric layout of bolt joints used in Ref. [17] in which the measured friction force includes that at other surfaces, not only that at target surface. (d) Symmetric layout in this work where the measured friction force is equal to the resultant of those at two target surfaces.

The specimens are made of ASTM 304 stainless steel and fastened together with an M8 bolt. There are two measured contact regions in parallel. Each contact region is a 30×30 mm^2 square with a

10 mm diameter hole at the center. The moving specimens are connected to the bottom fixture by two pins with a diameter of 8 mm. There is a 1 mm gap (see the main view in Fig. 1(a)) between both sides of the protruding part in the middle of the bottom fixture and the moving specimen to avoid the effect of their contact on the measurements. The fixed specimen is specially designed to have greater flexibility along the normal direction of the contact surface, thereby avoiding as much as possible the tilt contact (or local contact which is found from wear scars in some tests [18]) between the moving and fixed surfaces caused by the extra moment during installation. The middle of the fixed specimen is made as a leaf spring, and the whole is like a dumbbell. This design idea is similar with the 'floating body approach' developed in Ref. [45]. From this point of view, the thinner the leaf spring, the more favorable the formation of plane contact. However, if the leaf spring is too thin, there is a risk of buckling instability in the test apparatus under large compressive loads. Therefore, considering the combined effects of the flexibility and structural stability, the thickness of the leaf spring is set to 3 mm. The other end of the fixed specimen is connected to the top fixture by two 8 mm diameter pins. Likewise, a 1 mm interval is reserved between the top fixture and the fixed specimen.

The top and bottom fixtures are mounted on a servo-hydraulic fatigue testing system (capacity 250 kN, Instron Inc.). There is a cylindrical depression at the upper end of the top fixture and the lower end of the bottom fixture, which is used to match with the boss of the piston shaft so that the axis of the fixtures coincides with the piston axis as much as possible. The piston shaft drives the moving specimens to reciprocate and causes relative motion of the bolted joint interfaces. The friction force induced by the relative motion is measured by a built-in load cell of the testing system. Note that the measured force is the resultant of the tangential contact forces on the two surfaces, as shown in Fig. 1(d). The relative displacement between the moving and fixed specimens is measured using a combination of a laser vibrometer (OFV-525, Polytec Inc.) and a small prism (size 10×10×10 mm) with a inclination of 45°. The prism is attached to the fixed specimen close to the contact area and is used to reflect the laser beam onto the end of the moving specimen where a reflective paper is pasted, as shown in Fig. 1(b). The laser spot is focused as close as possible to the contact surface. It is worth noting that since the bolted joint specimen is not strictly constrained along the normal direction of the contact surface, the piston oscillation excitation may cause the specimen to slightly vibrate along the normal direction. Therefore, to eliminate the influence of this factor on the displacement measurement accuracy, the path of the laser beam is set parallel to the contact surface, see Fig. 1(b). Another point to note is that due to the compliance of the leaf spring, the relative movement between the prism and the ideal measurement point (on the same side as the reflective paper and close to the contact surface) on the fixed specimen should not be ignored when measuring the relative displacement of the target interface. This issue will be discussed in Section 2.2. In addition, the bolt preload is recorded by an annular force washer (KMR-40 kN for M8 bolt, HBM Inc.). It should be pointed out that the present test apparatus is semi-closed loop controlled. The controlled variable is the piston displacement, not the measured interface relative displacement.

Before each test, the target surfaces are cleaned with acetone and dried. At the same time, the topography of all contact surfaces is measured using an Alicona Infinite Focus instrument and will be employed to estimate the parameters of the multi-scale contact model in Section 3. All tests were carried at room temperature. The test procedure is given as follows:

(1) Mount the fixtures on the servo-hydraulic testing system, and then assemble the fixed and moving specimens on the top and bottom fixture using two pins, respectively;

(2) Drive the moving part upward by the piston shaft until the bolt holes on the fixed and moving specimens are aligned, then assemble the fixed and moving specimens using an M8 bolt, a square nut, and the force washer;

(3) Tighten the bolt and monitor the preload by the force washer until reaching up to a target value (the applied preload deviates from the target by ±5% due to hand tightening), and then adjust the position of the laser vibrometer so that the laser spot is focused on the set measurement point;

(4) apply a harmonic displacement with a frequency of 5 Hz along the piston axis to the moving specimens, at the same time, record the friction force, the relative displacement between the fixed and moving specimens, and the bolt preload.

2.2 Experimental results

As mentioned above, although the prism and the ideal measurement position on the fixed specimen are in close proximity (about 7 mm), the high compliance of the leaf spring in the middle of the fixed specimen may have a significant effect on the displacement measurement. Therefore, to quantify this compliance and further correct the measured displacements, a finite element model of the fixed specimen was established, as shown in the inset in Fig. 2(a). The model takes into accounts the fillets and structural elastic deformation. A mechanical analysis was carried out and the relative displacement between the prism and the ideal measurement position as a function of compression load is depicted in Fig. 2(a). It shows that the compliance of the leaf spring between the prism and the ideal measurement position is 0.34 μm/kN. All measured relative displacement data are corrected by subtracting the product of the compliance and measured force.

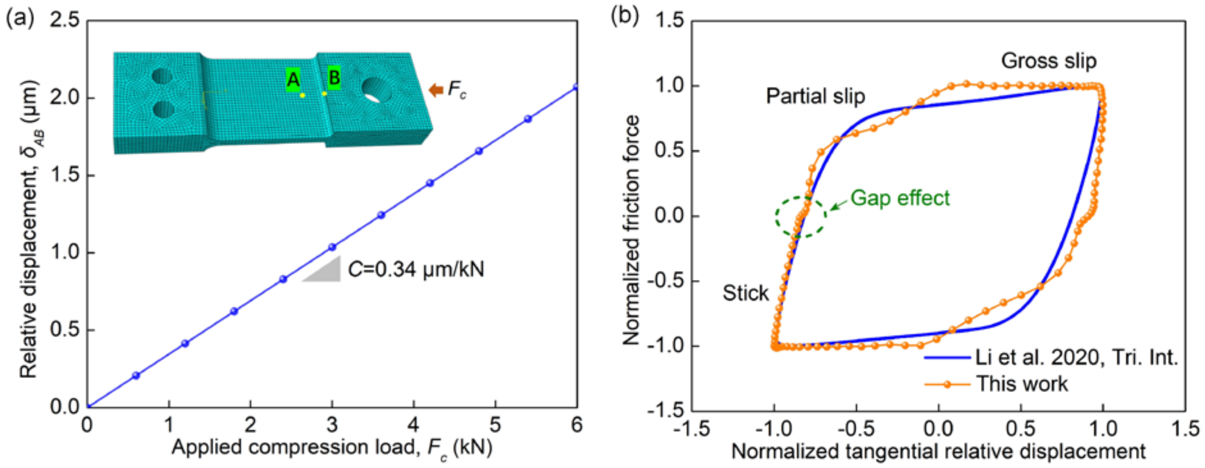

Fig. 2 (a) Relative displacement between points A and B as a function of the applied compression load. Points A and B represent laser spots on the prism and the ideal measurement position on the fixed specimen, respectively. (b) Comparison of the normalized hysteresis loops measured in this work with that in Ref. [17]. Normalization is implemented by dividing the original measurement data by the corresponding amplitude.

Figure 2(b) compares a typical hysteresis loop measured by the present test apparatus with that obtained in Ref. [17] where an asymmetric specimen with an M6 bolt was tested. For a more intuitive comparison, the original hysteresis loops were normalized by dividing by the amplitude of force/displacement. Taking the loading stage as an example, it can be seen that the contact surface in Ref. [17] experiences stick, partial slip, and gross slip successively. The force-displacement curve looks smooth and the tangential contact stiffness decreases monotonically with increasing relative displacement.

By contrast, the force-displacement curve measured in this work exhibits a complex shape after the initial stick regime, and there are three distinct reductions in the tangential contact stiffness. The first reduction occurs at zero friction force, where the friction force hardly changes with the increase of the interface relative displacement. It means that there are gaps in the load transmission path of the test apparatus. These gaps are most likely to exist at the pin connections between the fixture and the specimen. Although the gap effect results in a temporary loss of the 'measured contact stiffness', it does not affect the energy dissipation per cycle. The second noticeable reduction occurs during the partial slip regime. The reason for this may be that one of the contact surfaces grossly slips while the other is still in the partial slip regime. Due to the difference in microscopic surface topography, even if the two contact surfaces are distributed symmetrically and synchronously loaded, it is impossible to maintain the same motion state. The third noticeable reduction occurs in the final stage of loading, which is caused by the gross slip of both contact surfaces. It can be found that during the gross slip regime, the tangential contact stiffness is zero (no residual stiffness), different from that in Ref. [17]. This result also corroborates our design idea for the test apparatus.

Figure 3(a) depicts the measured hysteresis loops under the same bolt preload of 11 kN but with different excitation amplitudes (A_{amp} =185 μm, 205 μm, and 225 μm). The excitation amplitude is obtained from the piston displacement. Each test was run for 50 cycles, during which the testing system stabilized after 20 cycles. Although the tangential relative motion of the bolted joint specimen leads to the preload oscillation, this change does not exceed ±5% of the initial value throughout test period. It can be found that under varying excitation amplitudes, the initial tangential contact stiffness (the slope of the red line in Fig. 3(a)) hardly changes, and so does the friction coefficient (which equals the ratio of friction force in the gross slip regime to the bolt preload). In addition, at the end of the gross slip phase, an 'uplift' (the friction force suddenly increases) in the hysteresis curve for the case A_{amp} =185 μm can be observed. The cause for this phenomenon is the contact between the screw and the bolt hole. Specifically speaking, when tightening the bolt, it is hard to control the position of the screw relative to the bolt hole. In some cases, the screw is too close to the inner wall of the bolt hole after tightening. Once the sliding distance of the contact surface exceeds the gap between the screw and the hole, a new contact will be formed between them and result in the 'uplift' phenomenon. This phenomenon is also observed in Refs. [17][35].

Figure 3(b) plots the ratio of friction force to bolt preload as a function of the tangential relative displacement under varying bolt preloads and excitation amplitudes. The shapes of the hysteresis curves for the given four scenarios are similar. The ratio of friction force in gross slip regime to the bolt preload (i.e. twice the friction coefficient of contact surface) varies with the bolt preload. This change may be caused by the evolution of the surface topography due to multiple tests.

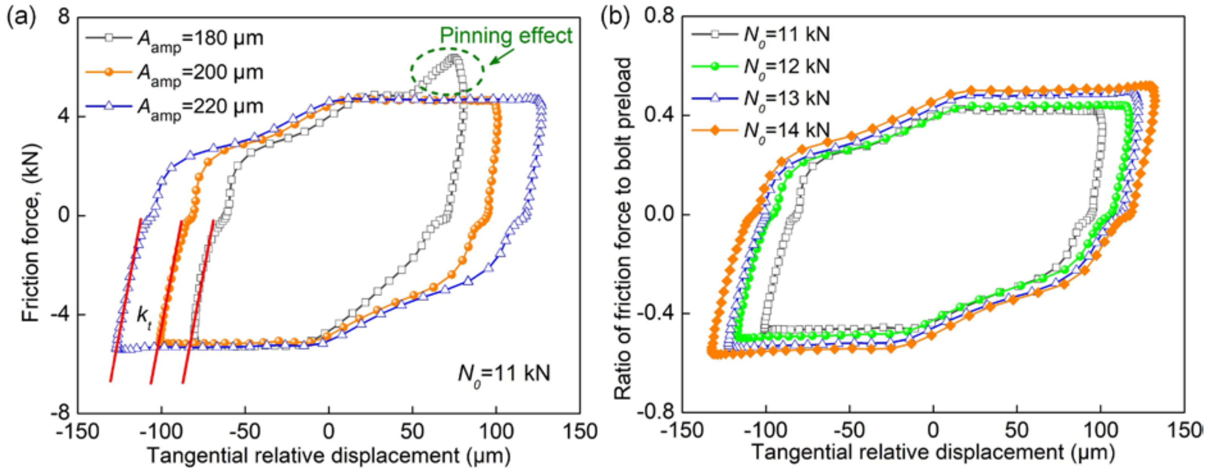

Fig. 3 (a) Friction force as a function of tangential relative displacement for varying excitation amplitudes and the same bolt preload of 11 kN. The slope of the red lines in the stick regime represents the tangential contact stiffness. (b) The ratio of friction force to bolt preload versus tangential relative displacement for varying loading cases: N_0=11 kN, A_{amp}=200 μm; N_0=12 kN, A_{amp}=225 μm; N_0=13 kN, A_{amp}=240 μm; N_0=14 kN, A_{amp}=260 μm.

The test rig developed in this paper can well avoid the influence of other contact surfaces other than the target surface on friction force measurement, which makes it highly accurate and unconventional among the fretting test rigs found in the literature so far. In the next section, a multi-scale modeling method will be developed to reproduce the initial tangential contact stiffness and the friction hysteresis behavior. Then in Section 4, the above experimental results will be used as a benchmark to verify the multi-scale contact model.

3 Modeling method

In this section, we propose a multi-scale modeling method based on fractal contact theory [46][47] and a discretized Iwan model to characterize the friction contact behavior of bolted joint interfaces. Fractal contact theory is used to consider the roughness characteristics of contact surfaces and to model the initial tangential contact stiffness, while the discretized Iwan model is used to reproduce the friction hysteresis behavior. The former provides necessary model parameters for the latter.

The fractal contact theory implicitly assumes that the contact pressure in flat-on-flat contact problems is uniformly distributed, which cannot be directly applied to bolted joint interface in which contact pressure monotonically decreases from a maximum value near bolt hole to zero at contact edge. Clearly, the area near the contact edge is easier to slide than the area near the contact center. Therefore, to improve accuracy, the non-uniform distribution of contact pressure is considered in the proposed modeling method. we divides the contact area into several parts and assumes a constant contact pressure in the divided local area, in which the fractal contact theory can be used.

3.1 Contact pressure distribution

The contact pressure distribution of bolted joint interfaces is related to many factors, such as the thickness of the connected parts, surface waviness, assembly process, etc. It is hard to obtain an analytical formation of the contact pressure distribution. Therefore, a widely accepted approximation function of the contact pressure distribution is used, which assumes that the contact pressure decreases linearly in the radial direction and is unchanged in the circumferential direction [48][49], as shown in Fig. 4.

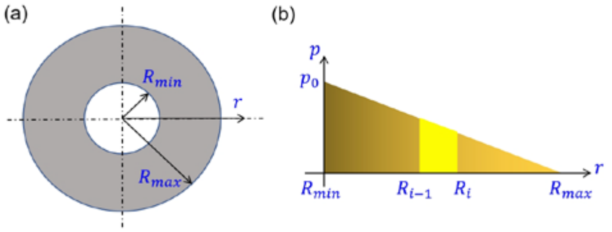

Fig. 4 (a) Nominal contact area of bolted joint interface, and (b) approximated contact pressure distributed along the contact radius.

The contact pressure $p(r)$ distributed along the contact radius can be expressed as

$$p(r) = p_0\left(\frac{R_{max} - r}{R_{max} - R_{min}}\right), \tag{1}$$

where R_{min} and R_{max} represent the radius of bolt hole and contact radius, respectively, r the distance to the hole center, p_0 the maximum pressure. The relationship between the bolt preload N_0 and the contact pressure function satisfies,

$$N_0 = \int_{R_{min}}^{R_{max}} 2\pi r p(r)\,\mathrm{d}r. \tag{2}$$

Substituting Eq. (1) into Eq.(2) yields the maximum contact pressure,

$$p_0 = \frac{3N_0}{\pi(R_{max}^2 + R_{max}R_{min} - 2R_{min}^2)}. \tag{3}$$

The distribution of contact pressure determines the frictional state (sticking or sliding) of the local contact region. To consider the effect of contact pressure distribution on the friction contact, we divide the contact area equally into h annular sub-regions along the contact radius. The radial length of each annular region equals $(R_{max} - R_{min})/h$. The normal load N_{0i} of the *i*th annular region can be expressed as

$$N_{0i} = \int_{R_{i-1}}^{R_i} 2\pi r p(r)\,\mathrm{d}r = \frac{2\pi p_0}{R_{max} - R_{min}}\left[\frac{R_{max}(R_i^2 - R_{i-1}^2)}{2} - \frac{(R_i^3 - R_{i-1}^3)}{3}\right], \tag{4}$$

where the boundaries of the *i*th annular region are (see Fig. 4(b)),

$$R_{i-1} = R_{min} + \frac{i-1}{h}(R_{max} - R_{min}), \tag{5}$$

$$R_i = R_{min} + \frac{i}{h}(R_{max} - R_{min}). \tag{6}$$

In each divided annular region, the contact pressure is assumed to be uniformly distributed. Therefore, the fractal contact theory can be applied to analyze the contact area of the bolted joint interface and further calculate the tangential contact stiffness.

3.2 Multi-scale contact model

When two rough flat surfaces are in contact, it can be simplified to a contact between a rough surface and a rigid smooth surface, as shown in Fig. 5, where a graphical representation of the simplified contact and the deformation geometry of an individual asperity are given. Considering the multi-scale nature of surface topography of rough surfaces, the fractal theory is used to describe the random rough features of connected surfaces. For completeness, the essential steps will be briefly reviewed below. Then it is combined with the contact mechanics model of individual asperity to simulate the normal and tangential contact.

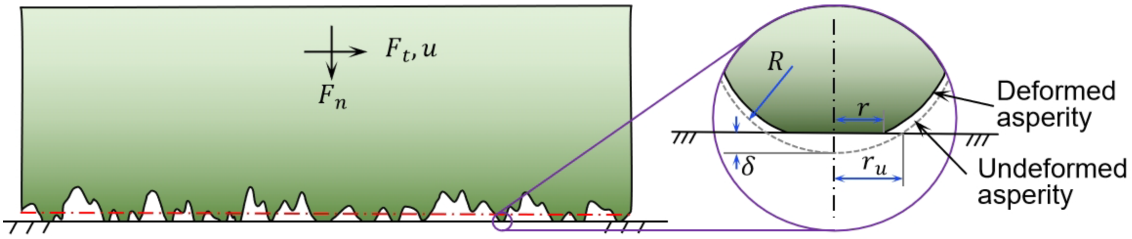

Fig. 5 Schematic diagram of the contact between a random rough surface and a rigid smooth surface, and the deformation geometry of an individual asperity.

The modified Weierstrass-Mandelbrot (W-M) function [47] is widely used to characterize a three-dimensional surface topography of random rough surfaces. For simplicity, we employ a simplified W-M function to describe the rough surface height $z(x)$,

$$z(x) = L\left(\frac{G}{L}\right)^{D-2}(\ln\gamma)^{0.5}\sum_{n=0}^{n_{max}}\gamma^{(D-3)n}\left[\cos\phi_{1,n} - \cos\left(\frac{2\pi\gamma^{n}x}{L} - \phi_{1,n}\right)\right], \tag{7}$$

where L denotes the sampling length of surface profile, G the fractal roughness, D the fractal dimension ($2<D<3$), γ the scaling factor that is related to the frequency spectrum of surface profile (typically $\gamma = 1.5$), n the frequency index and n_{max} corresponding to the high cutoff frequency of the profile, $\phi_{1,n}$ the random phase, and x the coordinate along the surface. The deformation of an individual asperity can be expressed as

$$\delta = 2G^{D-2}(\ln\gamma)^{0.5}(2r_u)^{3-D}, \tag{8}$$

where r_u is the truncated radius of the undeformed asperity (see the local enlarged view in Fig. 5).

According to the deformation geometry of an individual asperity, $R^2 - (R-\delta)^2 = r_u^2$ and $R \gg \delta$, the curvature radius R of the asperity can be derived as

$$R = 2^{D-5}G^{2-D}(\ln\gamma)^{-0.5}\left(\frac{a_u}{\pi}\right)^{0.5D-0.5}, \tag{9}$$

where a_u is the truncated area of the undeformed asperity and equals $a_u = \pi r_u^2$.

3.2.1 Normal contact

Under a certain normal load, the asperities of the rough surface with different heights will generally be in three deformation states, including purely elastic, elastic-plastic, and fully plastic deformations, denoted by the subscripts e, ep, and p, respectively. Therefore, the asperities undergo different normal loads, deformations, and contact areas, from each other.

(1) Purely elastic contact

When the height of the asperity is low (namely, the deformation of the asperity is relatively small), the asperity is in a purely elastic deformation state. According to Hertz contact theory [50], the contact force F_e can be expressed as

$$F_e = \frac{4}{3} E^* R^{0.5} \delta^{1.5}, \tag{10}$$

where E^* is the reduced elastic modulus, $E^* = \left[\left(1-{\vartheta_1}^2\right)/E_1 + \left(1-{\vartheta_2}^2\right)/E_2\right]^{-1}$ with ϑ_1, E_1, ϑ_2, and E_2 being the Poisson's ratios and elastic moduli of two contacting bodies. Substituting Eqs. (8) and (9) into Eq. (10) yields the relationship between the contact force F_e and the truncated contact area a_u,

$$F_e(a_u) = \frac{2^{5.5-D}}{3\pi^{2-0.5D}} E^* G^{D-2} (\ln\gamma)^{0.5} {a_u}^{2-0.5D}. \tag{11}$$

(2) Fully plastic contact

When the asperity is relatively high, the fully plastic deformation of the asperity occurs. Based on Ref. [22], the contact force F_p can be expressed as

$$F_p(a_u) = 2\pi R H \delta = \eta \sigma_y a_u, \tag{12}$$

where H is the hardness of softer material and equals $H = \eta\sigma_y$ (typically η=2.79) with σ_y being the yield strength.

(3) Elastic-plastic contact

When the height of the asperity is moderate, the asperity is in a transition from the purely elastic deformation to the fully plastic deformation. Following Ref. [51], the contact force F_{ep} induced by the elastic-plastic deformation of asperity is

$$F_{ep} = k_\vartheta H \pi R {\delta_{ec}}^{-\beta} \delta^{1+\beta}, \tag{13}$$

where k_ϑ is the mean contact pressure factor, δ_{ec} the critical deformation at which plastic yielding begins, and $\beta = \ln(2/k_\vartheta)/\ln\left(\delta_{pc}/\delta_{ec}\right)$ in which δ_{pc} the critical deformation at the beginning of fully plastic deformation and equals $\delta_{pc} = 110\delta_{ec}$ [51]. According to Ref. [52], k_ϑ can be expressed as a function of Poisson's ratio,

$$k_\vartheta = 0.3097 + 0.2094\vartheta + 0.1295\vartheta^2. \tag{14}$$

The critical deformation δ_{ec} at onset of plastic yielding is given, based on Ref. [53],

$$\delta_{ec} = \left(\frac{0.75\pi k_{\vartheta} H}{E^*}\right)^2 R. \tag{15}$$

Then, substituting Eqs.(8, 9, and 15) into Eq.(13), the expression of the normal force F_{ep} as a function of the truncated contact area a_u can be obtained,

$$F_{ep}(a_u) = 2^{13\beta-2\beta D-1}\left(\frac{E^*}{3}\right)^{2\beta} \pi^{\beta(D-4)}(k_{\vartheta}H)^{1-2\beta}G^{2\beta(D-2)}(\ln\gamma)^{\beta}{a_u}^{1+2\beta-\beta D}. \tag{16}$$

The reason why the contact forces F_e, F_{ep}, and F_p are expressed as a function of the truncated area a_u is that the total contact force F_n can be obtained by integrating the product of the contact force of a single asperity and the area distribution function $n(a_u)$, as follows,

$$F_n = \begin{cases} \int_0^{a_{u\_p}} F_p n(a_u)\,\mathrm{d}a_u + \int_{a_{u\_p}}^{a_{u\_e}} F_{ep} n(a_u)\,\mathrm{d}a_u + \int_{a_{u\_e}}^{a_{u\_l}} F_e n(a_u)\,\mathrm{d}a_u, & a_{u\_l} > a_{u\_e} \\ \int_0^{a_{u\_p}} F_p n(a_u)\,\mathrm{d}a_u + \int_{a_{u\_p}}^{a_{u\_l}} F_{ep} n(a_u)\,\mathrm{d}a_u, & a_{u\_p} < a_{u\_l} < a_{u\_e} \\ \int_0^{a_{u\_l}} F_p n(a_u)\,\mathrm{d}a_u, & a_{u\_l} < a_{u\_p} \end{cases} \tag{17}$$

where the integral limits $a_{u\_p} = 2\pi R\delta_{pc}$, $a_{u\_e} = 2\pi R\delta_{ec}$, and a_{u_l} represents the maximum truncated area. The area distribution function $n(a_u)$ is given, according to Ref. [47],

$$n(a_u) = 0.5(D-1){a_{u\_l}}^{0.5D-0.5}{a_u}^{-0.5D-0.5}. \tag{18}$$

The maximum truncated area a_{u_l} of a single asperity can be expressed as a function of the real contact area A_r [24], as follows,

$$a_{u\_l} = 2\frac{3-D}{D-1}A_r. \tag{19}$$

Once the fractal and material parameters are known by measurement, the real contact area A_r can be obtained setting the normal force F_n (Eq. (17)) to be equal to the applied normal load N_{0i} (Eq. (6)) in the ith annular region of the bolted joint interface. A detailed expression of the normal force F_n is given in **Appendix A**. Then, the real contact area A_{ri} of the ith annular contact region is used as a known parameter to solve for the tangential contact.

3.2.2 Tangential contact stiffness

Similarly, we first consider the tangential friction contact of a single asperity. Then the tangential contact stiffness k_{ti} of the ith annular contact region can be determined by integrating the individual contact stiffness with the area distribution function $n(a_u)$. Note that the 'tangential contact stiffness' here refers to the initial value of the tangential contact stiffness at the onset of the stick regime of the contact interface. Mindlin [54] investigated the friction behavior of the contact between two elastic spheres (equivalent to a elastic sphere interacting with a rigid plane) and derived the elastic deformation of the sphere under a monotonic tangential load as

$$u=\frac{3\mu F_n}{16G^*r}\left[1-\left(1-\frac{F_t}{\mu F_n}\right)^{2/3}\right], \tag{20}$$

where μ, G^*, r, and F_t denote the friction coefficient, reduced shear modulus, contact radius, and tangential load, respectively, and $G^*=[(2-\vartheta_1)/G_1+(2-\vartheta_2)/G_2]^{-1}$. The tangential contact stiffness of a single asperity can be obtained by finding the limit of the derivative $\partial F_t/\partial u$ at $u\to 0$,

$$k_{t\_asp}=\lim_{u\to 0}\frac{\partial F_t}{\partial u}=\lim_{u\to 0}8G^*r\left(1-\frac{16G^*ru}{3\mu F_n}\right)^{1/2}=8G^*r. \tag{21}$$

According to Hertz contact theory and the deformation geometry of a single asperity, the contact radius can be determined by $r=\sqrt{a_u/2\pi}$. Substituting the contact radius into Eq. (21) yields the tangential contact stiffness of a single asperity as a function of the truncated area a_u,

$$k_{t\_asp}=4\sqrt{\frac{2}{\pi}}G^*{a_u}^{0.5}. \tag{22}$$

Finally, the tangential contact stiffness k_{ti} of the i^{th} annular contact region is determined by integrating the product of k_{t_asp} and the area distribution function,

$$k_{ti}=\int_{a_{u\_e}}^{a_{u\_l}}k_{t\_asp}n(a_u)\,\mathrm{d}a_u=\frac{4\sqrt{2}G^*(D-1)\psi^{1.5-0.5D}}{\sqrt{\pi}(2-D){a_{u\_l}}^{0.5-0.5D}}\left({a_{u\_l}}^{1-0.5D}-{a_{u\_e}}^{1-0.5D}\right). \tag{23}$$

3.3.3 Friction hysteresis

In dynamic modeling of joint structures such as turbine blade systems, the phenomenological models are frequently used to reproduce the friction hysteresis behavior of joint interfaces, due to their good compatibility with nonlinear dynamics analysis methods. On the other hand, when the local contact pressure is uniformly distributed, the contact surface is in the stick or slip regime under tangential load. This behavior can be well captured by the Jenkins element (a basic component of the Iwan model). Therefore, in this paper, the Iwan model is discretized to simulate the friction behavior by comprehensively considering the non-uniform contact pressure distribution and the surface rough characteristics, as shown in Fig. 6(a).

Different from the original Iwan model, the discretized Iwan model is composed of several Jenkins elements in parallel and each Jenkins element has the different stiffness k_{ti} and critical sliding force $f_i = \mu N_{0i}$, see Fig. 6(b and c). The stiffness k_{ti} is determined by the fractal contact theory (Eq. (23)), while the critical sliding force f_i depends on the normal load distribution function (Eq. (6)).

For a monotonic tangential loading case, the force-displacement relation of Jenkins element can be expressed as

$$F_{ti} = \begin{cases} k_{ti}u, & 0 < u \le \dfrac{f_i}{k_{ti}}. \\ f_i, & \text{else} \end{cases} \tag{24}$$

For the unloading and reloading cases, the friction force can be determined as

$$F_{ti} = \begin{cases} k_{ti}(u - u_0) + f_i, & u_0 \ge \dfrac{f_i}{k_{ti}}, \dot{u} < 0, u_0 - \dfrac{2f_i}{k_{ti}} < u \le u_0 \\ -f_i, & u_0 \ge \dfrac{f_i}{k_{ti}}, \dot{u} < 0, -u_0 < u \le u_0 - \dfrac{2f_i}{k_{ti}} \\ k_{ti}(u + u_0) - f_i, & u_0 \ge \dfrac{f_i}{k_{ti}}, \dot{u} > 0, -u_0 \le u < \dfrac{2f_i}{k_{ti}} - u_0 \\ f_i, & u_0 \ge \dfrac{f_i}{k_{ti}}, \dot{u} > 0, \dfrac{2f_i}{k_{ti}} - u_0 \le u < u_0 \\ k_{ti}u, & u_0 < \dfrac{f_i}{k_{ti}} \end{cases} \tag{25}$$

where $\dot{u}$ denotes the velocity and u_0 the amplitude of displacement. The total friction force can be obtained by

$$F_t = \sum_{i=1}^{i=h} F_{ti}. \tag{26}$$

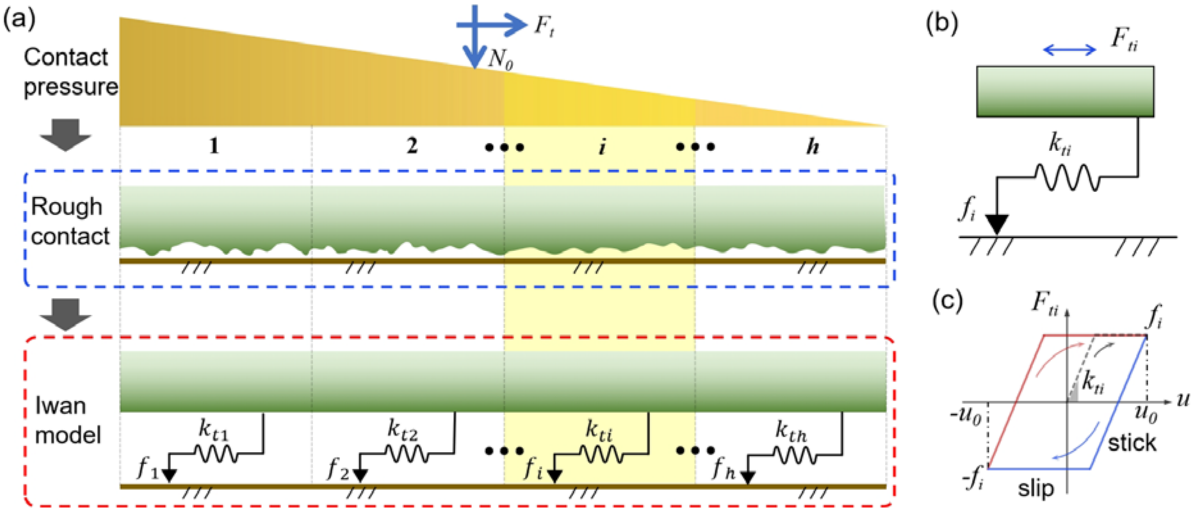

Fig. 6 (a) Schematic diagram of modeling the friction hysteresis behavior by considering the contact pressure distribution and rough contact in the Iwan model. (b) Jenkins element and (c) corresponding

force-displacement curve under periodic tangential loads. The blue and red curves represent the unloading and reloading cases, respectively.

4 Results and discussion

In this section, the effectiveness of the proposed multi-scale contact modeling method is validated by comparison with the experimental results in Section 2. Then, a parametric analysis is performed to discuss the effect of the number of the divided annular sub-regions on the model accuracy.

4.1 Model parameters estimation

To assess the capability of the developed multi-scale contact model to reproduce the friction contact of bolted joint interfaces, the first necessary step is to estimate model parameters. These parameters include contact radius R_{max}, fractal dimension D, fractal roughness G, and friction coefficient μ.

Refs. [19][55] investigated the contact pressure distribution at the interface of bolted joints using a direct measurement method (based on pressure film) and a finite element analysis method. The contact radius obtained by these two methods shows good agreement, with a relative error of less than 5%. Therefore, in this paper we employ the finite element contact analysis method to calculate the contact radius of the bolted joint interfaces. The finite element contact analysis was performed using the software Abaqus, and all components were meshed using 8-node linear hexahedron element (type C3D8R). The model has 31521 nodes, 25936 elements, and 1088 contact elements (only for each target contact surface). Figure 7(a) shows the contact pressure distribution obtained by finite element contact analysis and plots the contact radius as a function of the bolt preload. With the increase of bolt preload, the contact radius increases monotonically and slightly.

The fractal parameters, D and G, are identified using the PSD (Power Spectral Density) function method [56]. The logarithm of the PSD of surface profile can be expressed as

$$\log P(\omega) = (2D-7)\log\omega + (2D-4)\log G - \log(\ln\gamma) + (6-2D)\log\pi + (5-2D)\log 2, \tag{27}$$

where P denotes the PSD and ω the wavevector of surface profile. Once the PSD-wavevector curve of the surface profile height in the double logarithmic coordinate system is obtained, the fractal parameters, D and G, can be identified according to the following expression,

$$k_{PSD} = 2D - 7, \tag{28a}$$

$$b_{PSD} = (2D-4)\log G - \log(\ln\gamma) + (6-2D)\log\pi + (5-2D)\log 2, \tag{28b}$$

where k_{PSD} and b_{PSD} are the slope and intercept of the PSD-wavevector curve, respectively. These two parameters, k_{PSD} and b_{PSD}, can be directly determined from the fitted PSD-wavevector curve.

Before fretting tests, all contact surfaces are cleaned with acetone and then the surface topography is measured using an optical 3D measurement system (Alicona G4 Infinite Focus). Figure 7(c) shows the measured surface photography of the fixed specimen (set as an example), where the straight yellow lines (FB1-4) represent the measurement paths for the surface profile height. Figure 7(d) depicts the measured surface profile height as a function of the sampling length. The sampling length of the measurement paths is around 9 mm.

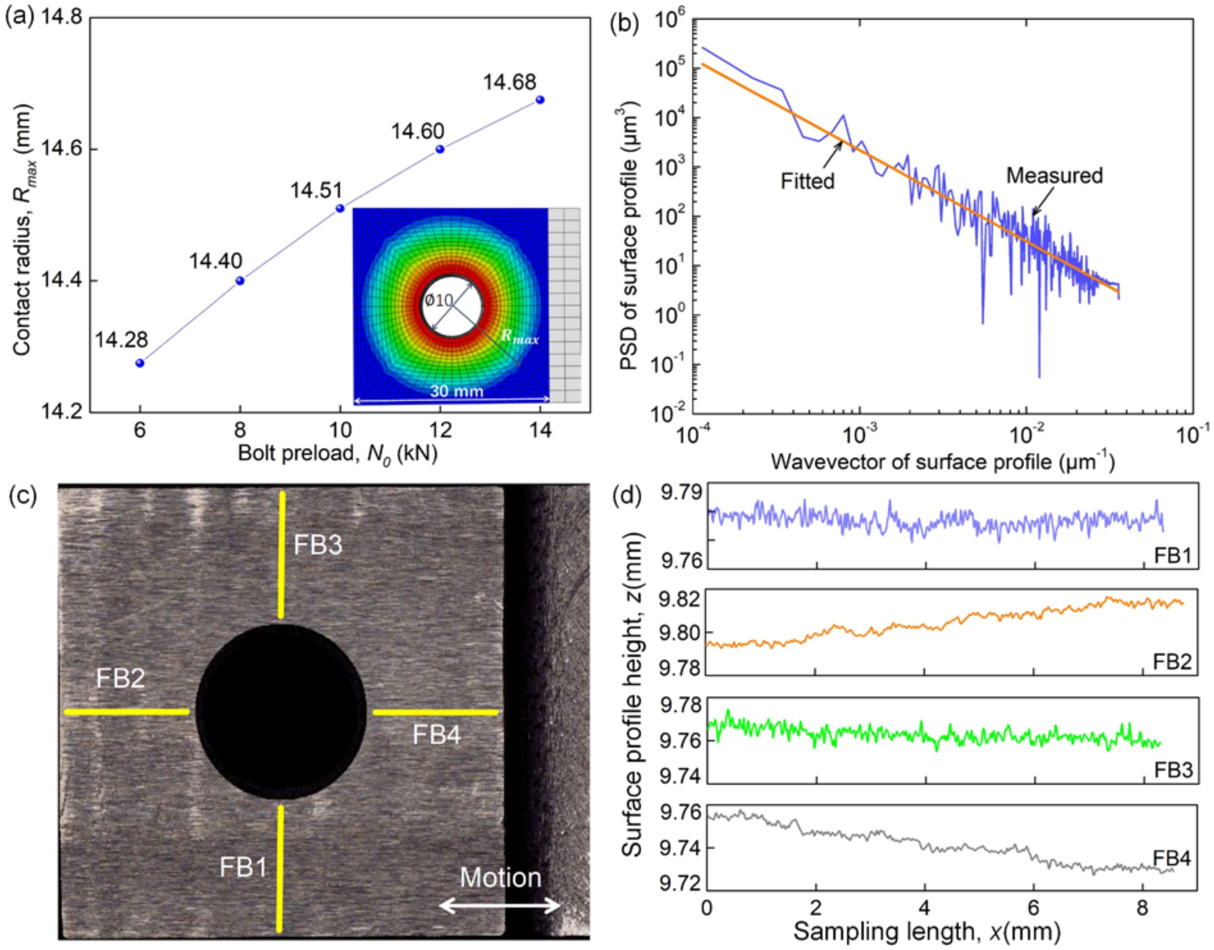

Fig. 7 (a) Contact radius R_{max} under different bolt preloads obtained from finite element contact analysis. The inset shows the finite element model for one of the specimens and the contact pressure distribution. (b) PSD curve of surface profile height (FB1 in Fig. 7c) in the double logarithmic coordinate system as a function of wavevector: measurement and least square fitting. (c) Surface photography measured by an optical 3D measurement system (Alicona G4 Infinite Focus). (d) Surface profile height curves at different measurement positions (FB1-4).

From the measured surface topography data, the surface roughness R_a and the PSD curve can be obtained. The average value of the measured roughness is regarded as the roughness of the contact surface. The PSD curve is fitted using the least square method, as shown in Fig. 7(b), where an example (FB1 in Fig. 7(c)) is given. Substituting the slope and intercept of the fitted PSD curve into Eq.(28) yields the fractal parameters. Table 1 lists the surface roughness R_a and fractal parameters, D and G, of the contact surfaces. Since the material of the connected specimens is the same and the surface roughness is close, the equivalent fractal parameters are determined using the average slope k_{PSD} and intercept b_{PSD} of all fitted PSD curves. Note that the fractal parameters cannot be averaged directly.

Table 1 Surface roughness and fractal parameters of contact surfaces. Moving_A$_{surf}$, Fixed_A$_{surf}$, Moving_B$_{surf}$, and Fixed_B$_{surf}$ represent contact surfaces of joint specimens. Interface_A and Interface_B represent the two target interfaces.

Surface roughness, R_a (μm)		Fractal parameters, D and G		
Moving_A$_{surf}$	1.28	Interface_A	D	2.523
Fixed_A$_{surf}$	1.39		G (m)	8.11×10^{-8}
Moving_B$_{surf}$	1.38	Interface_B	D	2.588
Fixed_B$_{surf}$	1.47		G (m)	3.25×10^{-9}

Friction coefficient μ is one of the parameters of the discretized Iwan model. This paper does not attempt to estimate the friction coefficient from the measured surface profile height. Therefore, to accurately predict the friction hysteresis response, the the friction coefficient is directly extracted from the measured hysteresis loops. The ratio of the friction force during the gross slip regime against the bolt preload is regarded as the friction coefficient. Moreover, the friction coefficients of two contact interfaces are assumed to be the same.

4.2 Model validation

This section is meant for validation of the developed multi-scale modeling method and quantization of model performance. The material parameters of the connected components are as follows: 200 GPa elastic modulus, 0.3 Poisson's ratio, 86 GPa shear modulus, and 205 MPa yield strength. Four experimental hysteresis curves under different loading conditions were selected for comparison with the simulation results. Besides, a comparison among the discretized Iwan models consisting of different numbers of Jenkins elements (or divided sub-regions) was also involved.

Figure 8 illustrates the simulated and the measured hysteresis curves for four different preloads. The approximate hexagonal hysteresis curves measured in the experiments can be well reproduced by the proposed contact model (h=4). The difference between the simulated and the measured results mainly appears in the partial slip stage of joint interfaces. The reasons for this difference are manifold. On one hand, after several tests, the surface topography changes due to the wear effect, and the cleaning operation (before each test) can only eliminate the influence of wear particles. It may lead to the deviation of the identified fractal parameters. On the other hand, the actual contact pressure distribution of the joint interface may differ from the assumption due to surface waviness and possible additional bending moments. In addition, the gap effect observed in the experiments was not considered in the contact model, and the actual friction coefficient of the two contact surfaces is also different. Nevertheless, given that the modeling approach is physics-based and multi-scale, these differences are acceptable to some extent. Comparing with the cases (h=1 and 2), the simulated results by the model (h=4) match better with the experimental results. A detailed analysis of the effect of the number of Jenkins elements (or divided sub-regions) on the model prediction capability is given in section 4.3.

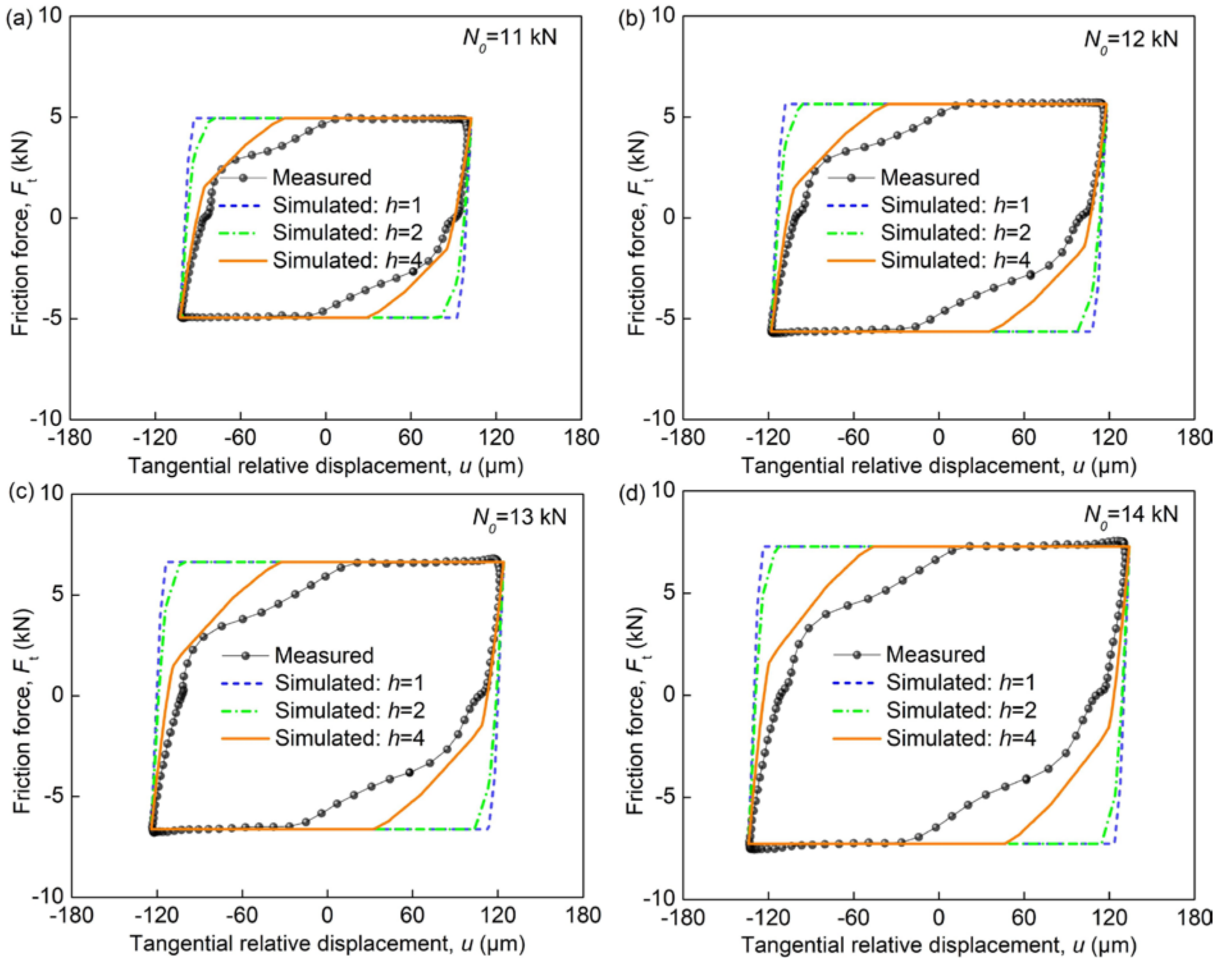

Fig. 8 Comparison of simulated hysteresis curves with experimental curves under different bolt preloads: (a) N_0=11 kN, (b) N_0=12 kN, (c) N_0=13 kN, (b) N_0=14 kN. The comparison among the models with different numbers (h=1, 2, and 4) of Jenkins elements is also involved.

To quantitatively evaluate the accuracy of the proposed modeling method, the equivalent real stiffness k_R (represents elastic stiffness) and the imaginary stiffness k_I (represents damping) are obtained according to the first-order Fourier expansion of the force-displacement curves [57]. As shown in Fig. 9, the equivalent real stiffness and imaginary stiffness obtained from the simulated curves are compared with those from the experimental curves. It can be seen that, except for the case of N_0=11 kN and 12 kN, where the relative difference of the the equivalent real stiffness is large (about 18%), the relative differences in the other comparisons are small (lower than 10%). Overall, the proposed multi-scale modeling method can reproduce the friction hysteresis behavior of bolted joint interfaces with acceptable accuracy.

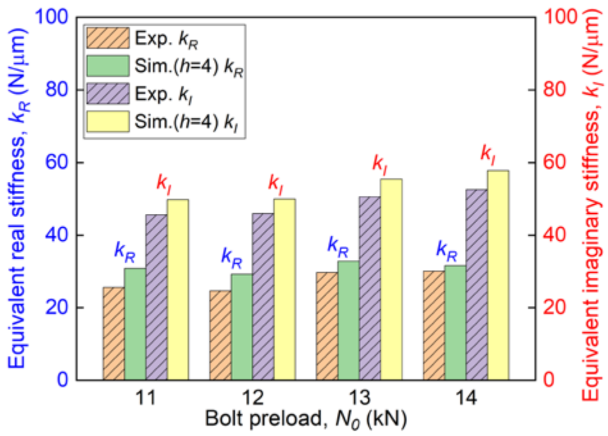

Fig. 9 Quantitative comparison of the simulated equivalent real stiffness k_{eq} and the equivalent imaginary stiffness k_I with the experimental counterparts under different bolt preloads.

4.3 Effect of the interface discretization

This section evaluates the effect of the number of the divided sub-regions (or the Jenkins elements) on the model performance over a wide range of displacement amplitudes. A simple case with only one contact surface is considered. The model parameters are as follows: contact radius R_{max}=15 mm, fractal dimension D=2.6, fractal roughness $G=1\times10^{-9}$, friction coefficient u=0.5, and bolt preload N_0=15 kN.

Figure 10 plots the equivalent real stiffness k_R and the imaginary stiffness k_I as a function of the relative displacement amplitudes. The comparison among the models with different numbers (h=1, 4, 7, and 10) of the divided sub-regions is also involved. With the increase of the number h, the difference in the equivalent stiffness predicted by different models becomes smaller and smaller. When the relative displacement amplitude is small, this difference is evident. In this case, the force-displacement curve predicted by the model with larger h is still a loop, while that obtained by the model with smaller h is a straight line (no hysteresis), see the inset in Fig.10(a). For the case of large displacement amplitude (>0.1 μm), the difference in equivalent stiffness predicted by different models (h=4, 7, and 10) is barely visible. It can be concluded that under the comprehensive consideration of the model complexity and the prediction accuracy, the model with h=4 is suitable for capturing the friction hysteresis behavior of bolted joint structures.

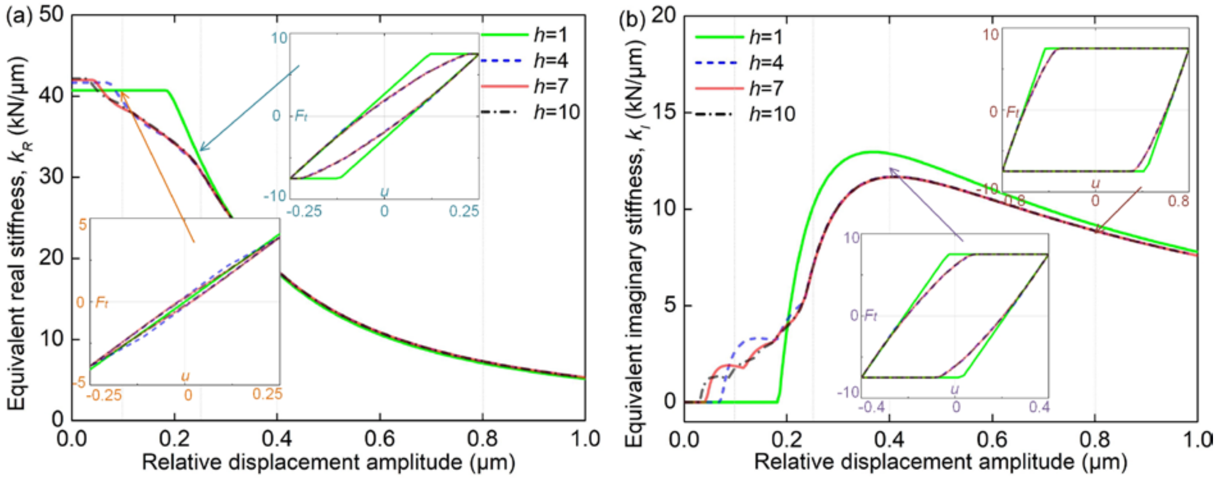

Fig. 10 (a) Equivalent real stiffness k_R and (b) equivalent imaginary stiffness k_I as a function of relative displacement amplitudes, obtained by the proposed modeling method with the different divided sub-regions (or the Jenkins elements).

5 Conclusions

In this paper, the tangential contact stiffness and friction hysteresis behavior of bolted joint interfaces were experimental and theoretically studied. In terms of experiments, a new test apparatus in which the joint specimens are arranged in a symmetric layout was developed to measure the friction force of bolted joint interfaces as purely as possible. In order to avoid the influence of additional moment generated during the installation process on the contact conditions of joint interfaces, the fixed specimen was designed to have high flexibility under the premise of ensuring the buckling stability of the entire assembly. The force-displacement curves under different loads were measured. The experimental friction hysteresis loops confirms the theoretical speculation about the origin of residual stiffness in Ref. [17] from the side.

A multi-scale contact modeling method was developed to reproduce the friction hysteresis behavior of bolted joint interfaces. This method comprehensively considers the multi-scale features of the randomly rough contact surface, the non-uniform distribution of contact pressure, and the convenience of the phenomenological contact model in simulating friction hysteresis, based on the fractal contact theory and the discretized Iwan model. The fractal contact theory was used to calculate the initial tangential contact stiffness of the jointed interface which is divided into several sub-regions for considering the contact pressure distribution. Then, a discretized Iwan model consisting of several Jenkins element with different contact stiffness (obtained from fractal contact analysis) and critical sliding forces was develop to describe the friction hysteresis. The effectiveness of the proposed method was verified comparing the simulation results with the experimental counterparts under different loading cases, which shows the potential for application to bolted joint structures.

It is worth emphasizing that in the fractal contact analysis the modeling of the initial tangential contact stiffness does not depend on the friction coefficient, so a physics-based model of friction coefficient could be incorporated into the method as a separate module in the future. The significance of this study is to provide structural engineers with a friction contact modeling approach for dynamic analysis of bolted joint structures without the need for complex contact experiments or dynamic testing in the initial design stage.

Declaration of Competing Interest

The authors declare that they have no known competing financial interests or personal relationships that could have appeared to influence the work reported in this paper.

Acknowledgments

This work was financially supported by China Postdoctoral Science Foundation (grant number 2022M712068), and the National Natural Science Foundation of China (grant numbers 12030215, 12121002, and 12072268). The authors thanks Prof. Muzio Gola (in Politecnico di Torino) for his valuable advice on the design of the test apparatus.

Appendix A: Formula for total normal force

If $a_{u\_l} > a_{u\_e}$, the normal load can be expressed as

$$F_n = \int_0^{a_{u\_p}} F_p n(a_u)\,\mathrm{d}a_u + \int_{a_{u\_p}}^{a_{u\_e}} F_{ep} n(a_u)\,\mathrm{d}a_u + \int_{a_{u\_e}}^{a_{u\_l}} F_e n(a_u)\,\mathrm{d}a_u. \tag{A1}$$

The first integral in Eq.(A1) represents the normal force of those asperities suffering from fully plastic deformation, which is equal to

$$F_{n\_p} = \frac{0.5\eta\sigma_y(D-1)}{1.5-0.5D} {a_{u\_l}}^{0.5D-0.5} {a_{u\_p}}^{1.5-0.5D}. \tag{A2}$$

The second integral represents the normal force caused by the elastic-plastic deformation of asperities and equals,

$$F_{n\_ep} = \left\{ \begin{array}{c} \frac{2^{13\beta-2\beta D-2}\pi^{\beta(D-4)}}{1.5+2\beta-\beta D-0.5D}(k_\vartheta H)^{1-2\beta} G^{2\beta(D-2)} (\ln\gamma)^{\beta}(D-1){a_{u\_l}}^{0.5D-0.5} \\ \times\left(\frac{E^*}{3}\right)^{2\beta}\left({a_{u\_e}}^{1.5+2\beta-\beta D-0.5D} - {a_{u\_p}}^{1.5+2\beta-\beta D-0.5D}\right) \end{array} \right\}. \tag{A3}$$

The third integral represents the normal force of those asperities in the purely elastic deformation,

$$F_{n\_e} = \frac{2^{4.5-D}E^* G^{D-2}(\ln\gamma)^{0.5}(D-1)}{(3\pi^{2-0.5D})(2.5-D)} {a_{u\_l}}^{0.5D-0.5}\left({a_{u\_l}}^{2.5-D} - {a_{u\_e}}^{2.5-D}\right). \tag{A4}$$

If $a_{u\_p} < a_{u\_l} < a_{u\_e}$, the normal load is expressed as

---

$$F_n = \int_0^{a_{u\_p}} F_p n(a_u)\,\mathrm{d}a_u + \int_{a_{u\_p}}^{a_{u\_l}} F_{ep} n(a_u)\,\mathrm{d}a_u$$

$$= \left\{ \begin{gathered} F_{n\_p} + \frac{2^{13\beta-2\beta D-2}\pi^{\beta(D-4)}}{1.5+2\beta-\beta D-0.5D}(k_\vartheta H)^{1-2\beta} G^{2\beta(D-2)} (\ln\gamma)^{\beta} (D-1) {a_{u\_l}}^{0.5D-0.5} \left(\frac{E^*}{3}\right)^{2\beta} \\ \times \left({a_{u\_e}}^{1.5+2\beta-\beta D-0.5D} - {a_{u\_p}}^{1.5+2\beta-\beta D-0.5D}\right) \end{gathered} \right\} \tag{A5}$$

If $a_{u\_l} < a_{u\_p}$, the normal load is expressed as

$$F_n = \int_0^{a_{u\_l}} F_p n(a_u)\,\mathrm{d}a_u = \frac{\eta \sigma_y (D-1) a_{u\_l}}{3-D} \tag{A6}$$

References

[1] Gaul L, Nitsche R. The role of friction in mechanical joints. ASME Appl Mech Rev, 2001; 54(2): 93-106. https://doi.org/10.1115/1.3097294

[2] De Benedetti M, Garofalo G, Zumpano M, Barboni R. On the damping effect due to bolted junctions in space structures subjected to pyro-shock. Acta Astronaut, 2007; 60(12): 947-956. https://doi.org/10.1016/j.actaastro.2006.11.011

[3] Bograd S, Reuss P, Schmidt A, Gaul L, Mayer M. Modeling the dynamics of mechanical joints. Mech Syst Signal Pr, 2011; 25(8): 2801-2826. https://doi.org/10.1016/j.ymssp.2011.01.010

[4] Mathis AT, Balaji NN, Kuether RJ, Brink AR, Brake MRW, Quinn DD. A review of damping models for structures with mechanical joints. ASME Appl Mech Rev, 2020; 72(4): 040802. https://doi.org/10.1115/1.4047707

[5] Ferrero J F, Yettou E, Barrau JJ, Rivallant S. Analysis of a dry friction problem under small displacements: application to a bolted joint. Wear, 2004; 256(11–12), 1135–1143. https://doi.org/10.1016/j.wear.2003.07.003

[6] Liu X, Sun W, Liu H, Du D, Ma H. Nonlinear vibration modeling and analysis of bolted thin plate based on non-uniformly distributed complex spring elements. J Sound Vib, 2022; 527: 116883. https://doi.org/10.1016/j.jsv.2022.116883

[7] Ouyang H, Oldfield MJ, Mottershead JE. Experimental and theoretical studies of a bolted joint excited by a torsional dynamic load. Int J Mech Sci, 2006; 48(12): 1447-1455. https://doi.org/10.1016/j.ijmecsci.2006.07.015

[8] Botto D, Umer M. A novel test rig to investigate under-platform damper dynamics. Mech Syst Signal Pr, 2018; 100: 344-359. https://doi.org/10.1016/j.ymssp.2017.07.046

[9] Wang Y, Ma Y, Hong J, Battiato G, Firrone CM. A Novel Test Rig for the Basic Nonlinear Characterization of Bolted Joints. Appl Sci, 2021; 11(12), 5613. https://doi.org/10.3390/app11125613

[10] Brake MRW, Schwingshackl CW, Reuß P. Observations of variability and repeatability in jointed structures. Mech Syst Signal Pr, 2019; 129, 282–307. https://doi.org/10.1016/j.ymssp.2019.04.020

[11] Botto D, Gastadi C, Gola MM, Umer M. An experimental investigation of the dynamics of a blade with two under-platform dampers. J Eng Gas Turbines Power, 2018; 140(3). https://doi.org/10.1115/1.4037865

[12] Gaul L, Lenz J. Nonlinear dynamics of structures assembled by bolted joints. Acta Mechanica, 1997; 125(1): 169-181. https://doi.org/10.1007/BF01177306

[13] Eriten M, Polycarpou AA, Bergman LA. Development of a lap joint fretting apparatus. Exp Mech, 2011; 51(8): 1405-1419. https://doi.org/10.1007/s11340-010-9458-8

[14] Ungar EE. The status of engineering knowledge concerning the damping of built-up structures. J Sound Vib, 1973; 26(1): 141-154. https://doi.org/10.1016/S0022-460X(73)80210-X

[15] Hartwigsen CJ, Song Y, McFarland DM, Bergman LA, Vakakis AF. Experimental study of non-linear effects in a typical shear lap joint configuration. J Sound Vib, 2004; 277(1-2): 327-351. https://doi.org/10.1016/j.jsv.2003.09.018

[16] Eriten M, Polycarpou AA, Bergman LA. Effects of surface roughness and lubrication on the early stages of fretting of mechanical lap joints. Wear, 2011; 271(11-12): 2928-2939. https://doi.org/10.1016/j.wear.2011.06.011

[17] Li D, Xu C, Botto D, Zhang Z, Gola MM. A fretting test apparatus for measuring friction hysteresis of bolted joints. Tribol Int, 2020; 151: 106431. https://doi.org/10.1016/j.triboint.2020.106431

[18] Li D, Xu C, Li R, Zhang W. Contact parameters evolution of bolted joint interface under transversal random vibrations. Wear, 2022; 500: 204351. https://doi.org/10.1016/j.wear.2022.204351

[19] Zhao B, Wu F, Sun K, Mu X, Zhang Y, Sun Q. Study on tangential stiffness nonlinear softening of bolted joint in friction-sliding process. Tribol Int, 2021; 156: 106856. https://doi.org/10.1016/j.triboint.2021.106856

[20] Eriten M, Polycarpou AA, Bergman LA. Physics-based modeling for fretting behavior of nominally flat rough surfaces. Int J Solids Struct, 2011; 48(10): 1436-1450. https://doi.org/10.1016/j.ijsolstr.2011.01.028

[21] Kang H, Li Z M, Liu T, Zhao G, Jing J, Yuan W. A novel multiscale model for contact behavior analysis of rough surfaces with the statistical approach. Int J Mech Sci, 2021; 212: 106808. https://doi.org/10.1016/j.ijmecsci.2021.106808

[22] Chen J, Zhang J, Hong J, Zhu L. Modeling tangential contact of lap joints considering surface topography based on Iwan model. Tribol Int, 2019; 137: 66-75. https://doi.org/10.1016/j.triboint.2019.04.031

[23] Wang R, Zhu L, Zhu C. Research on fractal model of normal contact stiffness for mechanical joint considering asperity interaction. Int J Mech Sci, 2017; 134: 357-369. https://doi.org/10.1016/j.ijmecsci.2017.10.019

[24] Shi W, Zhang Z. Contact characteristic parameters modeling for the assembled structure with bolted joints. Tribo Int, 2022; 165: 107272. https://doi.org/10.1016/j.triboint.2021.107272

[25] Liu J, Ma C, Wang S, Wang S, Yang B. Contact stiffness of spindle-tool holder based on fractal theory and multi-scale contact mechanics model. Mech Syst Signal Pr, 2019; 119: 363-379. https://doi.org/10.1016/j.ymssp.2018.09.037

[26] Yu X, Sun Y, Wu S. Multi-stage contact model between fractal rough surfaces based on multi-scale asperity deformation. Appl Math Model, 2022; 109: 229-250. https://doi.org/10.1016/j.apm.2022.04.029

[27] Armand J, Salles L, Schwingshackl CW, Süß D, Willner K. On the effects of roughness on the nonlinear dynamics of a bolted joint: a multiscale analysis. Eur J Mech A-Solid, 2018; 70: 44-57. https://doi.org/10.1016/j.euromechsol.2018.01.005

[28] Segalman DJ. A four-parameter Iwan model for lap-type joints. J Appl Mech, 2005; 72: 752-760. https://doi.org/10.1115/1.1989354

[29] Song Y, Hartwigsen CJ, McFarland DM, Vakakis AF, Bergman LA. Simulation of dynamics of beam structures with bolted joints using adjusted Iwan beam elements. J Sound Vib, 2004; 273(1-2): 249-276. https://doi.org/10.1016/S0022-460X(03)00499-1

[30] Li Y, Hao Z. A six-parameter Iwan model and its application. Mech Syst Signal Pr, 2016; 68: 354-365. https://doi.org/10.1016/j.ymssp.2015.07.009

[31] Biswas S, Chatterjee A. A two-state hysteresis model for bolted joints, with minor loops from partial unloading. Int J Mech Sci, 2018; 140: 506-520. https://doi.org/10.1016/j.ijmecsci.2018.03.021

[32] Li D, Botto D, Xu C, Liu T, Gola MM. A micro-slip friction modeling approach and its application in underplatform damper kinematics. Int J Mech Sci, 2019; 161: 105029. https://doi.org/10.1016/j.ijmecsci.2019.105029

[33] Abad J, Medel F J, Franco J M. Determination of Valanis model parameters in a bolted lap joint: Experimental and numerical analyses of frictional dissipation. Int J Mech Sci, 2014; 89: 289-298. https://doi.org/10.1016/j.ijmecsci.2014.09.014

[34] De Wit CC, Olsson H, Astrom KJ, Lischinsky P. A new model for control of systems with friction. IEEE T Automat Contr, 1995; 40(3): 419-425. https://doi.org/10.1109/9.376053

[35] Brake MRW. A reduced Iwan model that includes pinning for bolted joint mechanics. Nonlinear Dyn, 2017; 87(2): 1335-1349. https://doi.org/10.1007/s11071-016-3117-2

[36] Li D, Botto D, Xu C, Gola MM. A new approach for the determination of the Iwan density function in modeling friction contact. Int J Mech Sci, 2020; 180: 105671. https://doi.org/10.1016/j.ijmecsci.2020.105671

[37] Li D, Xu C, Kang J, Zhang Z. Modeling tangential friction based on contact pressure distribution for predicting dynamic responses of bolted joint structures. Nonlinear Dyn, 2020; 101(1): 255-269. https://doi.org/10.1007/s11071-020-05765-6

[38] Li C, Jiang Y, Qiao R, Miao X. Modeling and parameters identification of the connection interface of bolted joints based on an improved micro-slip model. Mech Syst Signal Pr, 2021; 153: 107514. https://doi.org/10.1016/j.ymssp.2020.107514

[39] Ahmadian H, Jalali H. Identification of bolted lap joints parameters in assembled structures. Mech Syst Signal Pr, 2007; 21(2): 1041-1050. https://doi.org/10.1016/j.ymssp.2005.08.015

[40] Yuan PP, Ren WX, Zhang J. Dynamic tests and model updating of nonlinear beam structures with bolted joints. Mech Syst Signal Pr, 2019; 126: 193-210. https://doi.org/10.1016/j.ymssp.2019.02.033

[41] Gimpl V, Fantetti A, Klaassen SWB, Schwingshackl CW, Rixen DJ. Contact stiffness of jointed interfaces: A comparison of dynamic substructuring techniques with frictional hysteresis measurements. Mech Syst Signal Pr, 2022; 171: 108896. https://doi.org/10.1016/j.ymssp.2022.108896

[42] Umer M, Botto D. Measurement of contact parameters on under-platform dampers coupled with blade dynamics. Int J Mech Sci, 2019; 159: 450-458. https://doi.org/10.1016/j.ijmecsci.2019.06.010

[43] Yang D, Lu ZR, Wang L. Parameter identification of bolted joint models by trust-region constrained sensitivity approach. Appl Math Model, 2021; 99: 204-227. https://doi.org/10.1016/j.apm.2021.06.017

[44] Jalali H, Ahmadian H, Mottershead JE. Identification of nonlinear bolted lap-joint parameters by force-state mapping. Int J Solids Struct, 2007; 44(25-26), 8087-8105. https://doi.org/10.1016/j.ijsolstr.2007.06.003

[45] Lavella M, Botto D, Gola MM. Design of a high-precision, flat-on-flat fretting test apparatus with high temperature capability. Wear, 2013; 302(1-2): 1073-1081. https://doi.org/10.1016/j.wear.2013.01.066

[46] Majumdar A, Bhushan B. Fractal model of elastic–plastic contact between rough surfaces. J Tribol, 1991;113 (1): 1–11. https://doi.org/10.1115/1.2920588

[47] Yan W, Komvopoulos K. Contact analysis of elastic-plastic fractal surfaces. J appl phys, 1998; 84(7): 3617-3624. https://doi.org/10.1063/1.368536

[48] Marshall MB, Lewis R, Dwyer-Joyce RS. Characterisation of contact pressure distribution in bolted joints. Strain, 2006; 42(1): 31-43. https://doi.org/10.1111/j.1475-1305.2006.00247.x

[49] Stephen JT, Marshall MB, Lewis R. An investigation into contact pressure distribution in bolted joints. Proc IMechE Part C: J Mech Eng Sci, 2014; 228(18): 3405-3418. https://doi.org/10.1177/0954406214528320

[50] Johnson KL. Contact mechanics. Cambridge university press, 1987.

[51] Kogut L, Etsion I. A finite element based elastic-plastic model for the contact of rough surfaces. Tribo T, 2003; 46(3): 383-390. https://doi.org/10.1080/10402000308982641

[52] Lin LP, Lin JF. An elastoplastic microasperity contact model for metallic materials. J Tribol, 2005; 127(3): 666-672. https://doi.org/10.1115/1.1843830

[53] Chang WR, Etsion I, Bogy DB. An elastic-plastic model for the contact of rough surfaces. J Tribol, 1987; 109(2):257-63. https://doi.org/10.1115/1.3261348

[54] Mindlin RD, Deresiewicz H. Elastic spheres in contact under varying oblique forces. J. Appl Mech, 1953; 20: 327-344. https://doi.org/10.1115/1.4010702

[55] Zhao B, Sun Q, Yang Y, Sun K, Liu Z. Study on interface non-uniform slip of combined rotor considering real preload distribution. Tribol Int, 2022; 169: 107482. https://doi.org/10.1016/j.triboint.2022.107482

[56] Pan W, Li X, Wang L, Guo N, Mu J. A normal contact stiffness fractal prediction model of dry-friction rough surface and experimental verification. Eur J Mech A-Solid, 2017; 66: 94-102. https://doi.org/10.1016/j.euromechsol.2017.06.010

[57] Gastaldi C, Gola MM. On the relevance of a microslip contact model for under-platform dampers. Int J Mech Sci, 2016; 115: 145-156. https://doi.org/10.1016/j.ijmecsci.2016.06.015